Radon backgrounds in the DEAP-1 liquid argon based Dark Matter detector

P.-A. Amaudruz[i], M. Batygov[c], B. Beltran[a], K. Boudjemline[b], M.G. Boulay[g], B. Cai[g], T. Caldwell[f], M. Chen[g], R. Chouinard[a], B.T. Cleveland[c], D. Contreras[h], K. Dering[g], F. Duncan[c], R. Ford[h], R. Gagnon[g], F. Giuliani[d], M. Gold[d], V.V. Golovko[g,1], P. Gorel[a], K. Graham[b], D.R. Grant[a], R. Hakobyan[a], A.L. Hallin[a], P. Harvey[g], C. Hearns[g], C.J. Jillings[c], M. Kuźniak[g], I. Lawson[h], O. Li[h], J. Lidgard[g], P. Liimatainen[h], W.H. Lippincott[j,2], R. Mathew[g], A.B. McDonald[g], T. McElroy[a], K. McFarlane[h], D. McKinsey[j], A. Muir[i], C. Nantais[g], K. Nicolics[g], J. Nikkel[j], T. Noble[g], E. O'Dwyer[g], K.S. Olsen[a], C. Ouellet[b], P. Pasuthip[g], T. Pollmann[g,3,*], W. Rau[g], F. Retiere[i], M. Ronquest[e], P. Skensved[g], T. Sonley[g], E. Vázquez Jáuregui[h], L. Veloce[g], M. Ward[g]

[a] *Department of Physics, University of Alberta, Edmonton, AB, T6G 2R3, Canada*
[b] *Department of Physics, Carleton University, Ottawa, ON, K1S 5B6, Canada*
[c] *Department of Physics and Astronomy, Laurentian University, Sudbury, ON, P3E 2C6, Canada*
[d] *Department of Physics, University of New Mexico, Albuquerque, NM 87131, USA*
[e] *University of North Carolina, Chapel Hill, NC 27517, USA*
[f] *Department of Physics, University of Pennsylvania, Philadelphia, PA 19104, USA*
[g] *Department of Physics, Engineering Physics and Astronomy, Queen's University, Kingston, ON, K7L 3N6, Canada*
[h] *SNOLAB, Lively, ON, P3Y 1N2, Canada*
[i] *TRIUMF, Vancouver, BC, V6T 2A3, Canada*
[j] *Department of Physics, Yale University, New Haven, CT 06511, USA*

Abstract

The DEAP-1 7 kg single phase liquid argon scintillation detector was op-

*Corresponding author.
Email address: tina@snolab.ca (T. Pollmann)
[1] Current address: AECL, Chalk River, ON, K0J 1J0, Canada.
[2] Current address: Fermilab, Batavia, IL 60510, USA.
[3] Current address: SNOLAB, Lively, ON, P3Y 1N2, Canada.

erated underground at SNOLAB in order to test the techniques and measure the backgrounds inherent to single phase detection, in support of the DEAP-3600 Dark Matter detector. Backgrounds in DEAP are controlled through material selection, construction techniques, pulse shape discrimination and event reconstruction. This report details the analysis of background events observed in three iterations of the DEAP-1 detector, and the measures taken to reduce them.

The ^{222}Rn decay rate in the liquid argon was measured to be between 16 and 26 µBq kg^{-1}. We found that the background spectrum near the region of interest for Dark Matter detection in the final DEAP-1 detector generation is well described considering events from three sources: radon daughters decaying on the surface of the active volume, the expected rate of electromagnetic events misidentified as nuclear recoils due to inefficiencies in the pulse shape discrimination arising from the prototype design, and leakage of events from outside the fiducial volume due to imperfect position reconstruction. These backgrounds statistically account for all observed events, and they will be strongly reduced in the DEAP-3600 detector due to its higher light yield and simpler geometry.

Keywords: Dark Matter, DEAP, liquid argon

---

1. Detection of Dark Matter with single phase argon detectors

Liquid argon offers significant advantages for dark matter detection. In particular it offers large target masses, exceptional purity, efficient scintillation, and pulse shape discrimination (PSD). Large Dark Matter detectors based on liquid argon have been proposed, including DEAP, MiniCLEAN [1],

WARP [2] and Dark Side [3].

Dark Matter particles with masses in the 10-1000 GeV range are expected to present in the detector as nuclear recoils at energies up to 100 keV. The most prevalent backgrounds in this energy range are from the beta decay of ^{39}Ar and from gamma and muon interactions. Electromagnetic backgrounds such as these can be suppressed by many orders of magnitude through PSD [4, 5, 6].

The argon scintillation light has a wavelength of 128 nm, which is not directly detectable with conventional PMTs. Nuclear recoils and electron recoils have different scintillation efficiencies in liquid argon. If the energy scale for nuclear-recoil-like events is denoted by the subscript "R" and the scale for electron-recoil-like events is denoted by the subscript "ee" then the nuclear recoil quenching factor, defined as E_R/E_{ee}, for liquid argon is about 0.25 [7].

2. The DEAP-1 detector

DEAP-1 was built as a prototype for the DEAP-3600 detector [8] currently under construction at SNOLAB [9]. It has been used to study the pulse shape discrimination power in liquid argon, detector backgrounds, and for prototyping components for the DEAP-3600 detector. Results from the initial run at Queen's University were previously reported [5]. Here, we report on the background studies done with three iterations of the DEAP-1 detector since the start of operation underground at SNOLAB.

The DEAP-1 detector is schematically shown in Fig. 1. The active volume is a cylinder, 28 cm long with a 15 cm diameter, defined by an acrylic

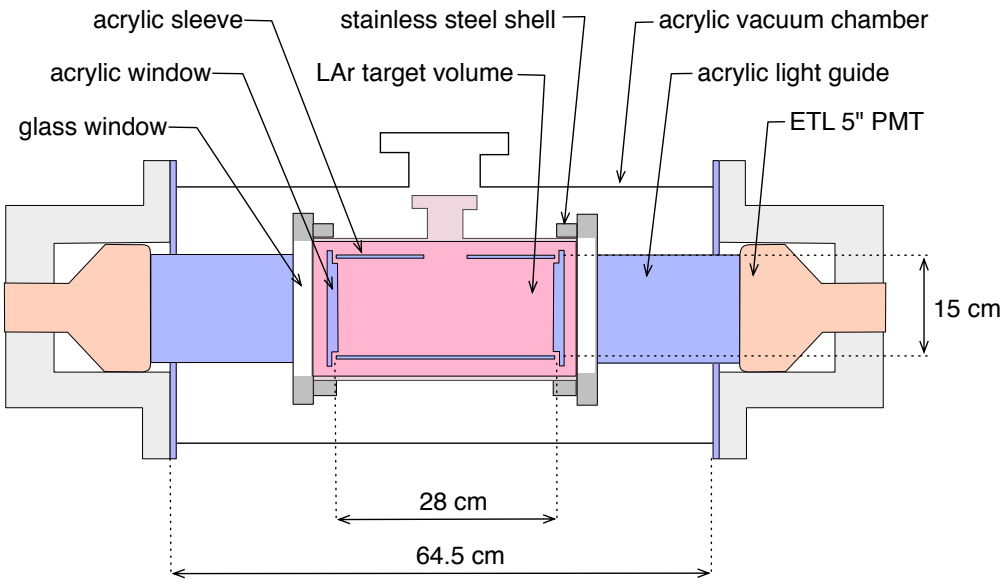

Figure 1: Schematic drawing of the DEAP-1 detector (G1). Different detector generations used different PMTs and different acrylic window configurations.

sleeve 0.64 cm thick, and closed off on each end with acrylic windows. The sleeve and acrylic windows are coated on the inside by vacuum deposition with the wavelength shifter 1,1,4,4-tetraphenyl-1,3-butadiene (TPB), which shifts the liquid argon scintillation light to a peak wavelength of 440 nm [10], where acrylic is transparent and photoelectron multiplier tubes (PMTs) are sensitive. The TPB layer is 1 µm to 3 µm thick.

The sleeve is covered by a teflon and Gore DR reflector and contained in a cylindrical stainless steel vessel with glass windows at each end. The total mass of liquid argon inside the vessel is 7.6 kg, with 7.0 kg in the active volume. Acrylic light guides with PMTs at their ends are attached to the glass windows. The light guides serve the dual purpose of absorbing radiation from the PMT glass and thermally insulating the PMTs from the liquid argon volume, thus allowing them to be operated at room temperature.

An opening at the top of the acrylic and stainless steel cylinders leads to the "neck", a pipe through which liquefied argon is filled into the detector. During normal operation argon gas flows up the neck, through a condenser, and back to the detector volume. The argon is purified only during the initial fill.

DEAP-1 went through three major iterations since the start of operations at SNOLAB. In the first generation, G1, 5 inch ETL 9390B (flat-face) PMTs were used. The acrylic windows loosely fit the acrylic sleeve, and the neck opening was 2.54 cm in diameter.

In the second generation, G2, the PMTs were replaced by Hamamatsu R5912 8 inch high quantum efficiency PMTs, which will be used in DEAP-3600. The light guides were replaced to accommodate the larger and differ-

ently shaped PMTs.

The third generation, G3, had a re-designed acrylic sleeve with a 0.64 cm radius neck opening covered with a plug that lets liquid argon in but prevents light generated in the neck from entering the active volume. The G3 windows were machined to fit tightly against the acrylic sleeve to prevent gaps through which scintillation light could enter the active target volume.

3. Background contributions to DEAP-1

Liquid argon is sensitive to ionizing radiation, including particles from cosmic rays, external and internal gammas and electrons, alpha particles, and neutrons. While all of these radiation types cause signals in the detector, nuclear-recoil-like signals at energies below 100 keV recoil energy directly compete with a possible WIMP signal. The other types of radiation cause background events only when misidentified as nuclear-recoil-like signals (PSD leakage).

External electromagnetic background from muons are reduced to $0.29\,\mathrm{m}^{-2}\,\mathrm{day}^{-1}$, by locating the DEAP-1 detector underground at SNOLAB at a depth of 6010 meters water equivalent [11].

Alpha particles exciting liquid argon produce a signal similar to nuclear recoils and are thus a source of background not discriminated by the PSD. We expect alpha particles from alpha emitting isotopes in the primordial ^{238}U and ^{232}Th decay chains to interact in the DEAP-1 and DEAP-3600 detectors through those isotopes' presence in detector and process system materials.

Both chains, partially shown in Fig. 2, contain radon isotopes which can emanate into the liquid argon and circulate through the process system. It

takes about 20 minutes for argon gas just above the chamber to circulate through the argon return and cooling lines. The ^{220}Rn from the thorium chain has a half-life of only 56 seconds and thus must emanate close to the detector chamber to produce background events. The ^{222}Rn from the uranium chain, with a half-life of 3.8 days, can reach the detector chamber from any emanation location in the system. Thus uranium-chain backgrounds are expected to dominate over thorium-chain backgrounds, unless the source of decay is in the chamber itself. This is unlikely as emanation from a cold surface like the argon acrylic chamber is reduced compared to emanation from a warm surface such as the gas return to the liquefier.

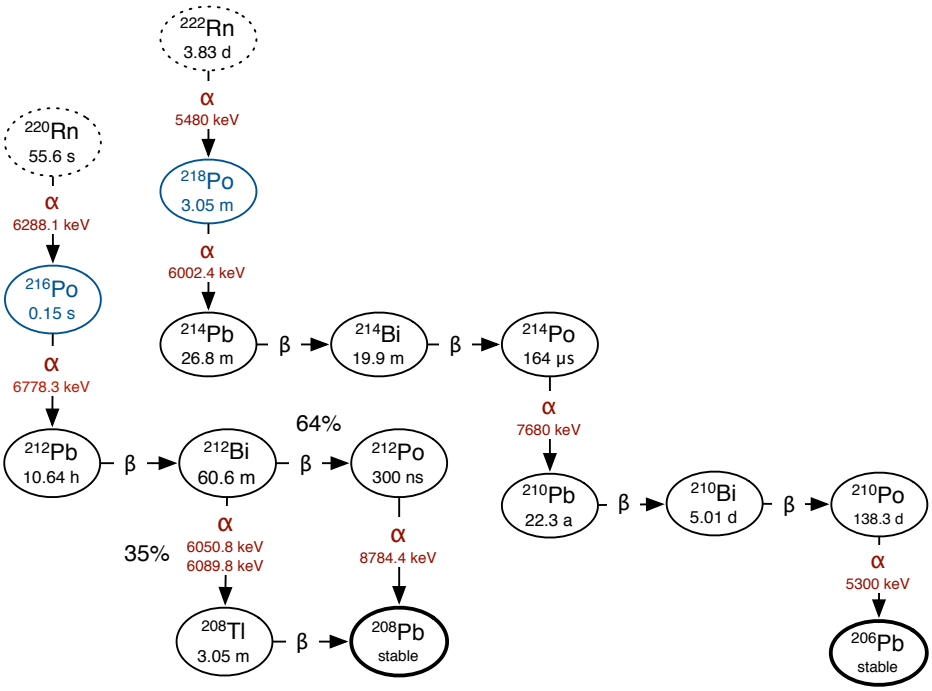

Figure 2: Decay chains of ^{220}Rn (from ^{232}Th) and ^{222}Rn (from ^{238}U) showing the relevant alpha decays for DEAP-1 and DEAP-3600.

The alpha particles from primordial isotope chains all have energies in excess of 5 MeV, much more than the WIMPs the experiment is designed to detect. Full energy alpha events, located in the active liquid argon volume where scintillation light is detected at high efficiency, can thus be readily discriminated based on their energy.

There are two scenarios in which the visible energy of an alpha particle is reduced, allowing it to appear in the energy region of interest for WIMP search. First, the event can occur at a location where the efficiency for collecting light is low, such as in the gap between the acrylic window and the acrylic sleeve or in the neck of the detector. Second, isotopes embedded in or adhering to the surface of the acrylic window or sleeve can alpha decay, resulting in reduced visible energy because the alpha particle loses energy in the acrylic or TPB layer before entering the liquid argon. In the second case, the recoil nucleus can also be emitted into the argon, causing a low energy nuclear recoil event.

Neutrons can reach the detector's active volume and induce a WIMP-like event. Because of the highly suppressed muon rate at SNOLAB, muon spallation induced neutrons are not a significant background source and neutrons produced in nuclear fission and (α, n) reactions, induced by alphas from the ^{238}U and ^{232}Th chains, become dominant. Samples of materials used in the construction of DEAP-1 were assayed for U/Th content in the SNOLAB Ge counter [12]. A GEANT 4 based Monte Carlo simulation was used to estimate the expected number of neutrons produced from these radioactive impurities. The rock wall neutron rate at SNOLAB was taken from Ref. [13]. The inner detector (steel chamber and PMTs) were calculated to produce less than 1

neutron/year. Neutron production in the aluminum dark-box, stainless steel stand for the water shield (see Sect. 4.3), and rock wall is expected to lead to a rate of about 10 n/year/kg at 30 $\mathrm{keV_{ee}}$ to 50 $\mathrm{keV_{ee}}$ in the fiducial volume of the detector (inner 10 cm, at 85% detection efficiency for nuclear recoils).

4. Background reduction measures

4.1. Chamber preparation

The inner acrylic chamber consists of the acrylic sleeve and the windows. The goal of a careful chamber preparation was to minimize the contamination of the detector surfaces with alpha emitting radon daughters.

The acrylic sleeve of DEAP-1 was machined out of commercially available acrylic stock from United Resins, Inc. The acrylic for the windows was acquired from Spartech Townsend Plastics. The radon diffusion length in acrylic is 0.11 mm [14], so a few millimetres of acrylic were machined off each surface of the chamber to remove radon daughters diffused into the material. From that point on, all preparation steps took place in a class 2000 cleanroom, and the exposure of the chamber to air was limited to roughly two hours, during which time the chamber was washed in an ultrasonic bath with detergent solution and then with ultra-pure water. The air activity in the cleanroom was measured to be 10 $\mathrm{Bq\,m^{-3}}$ of ^{222}Rn with a commercial RAD7 radon detector.

The chamber was then stored in a glove box purged with boil-off nitrogen at an overpressure equivalent to 2.5 cm of water. The glove box is constructed from materials with low radon emanation (acrylic, copper) and has radon impermeable seals (teflon, butyl rubber). The chamber was exposed to lab

air for ∼1 minute while moving it from the glove box to the TPB evaporator and back.

In order to remove the surface deposits and sub-surface implantation of ^{210}Po accumulated after machining, 20 µm of the acrylic windows and sleeve of G1 and G3 were sanded off with sand paper chosen for low U and Th contamination. The procedure was tried on acrylic test plates with scratches of calibrated depth and it was determined that manual wet sanding would remove the required amount of material. The pieces were washed with pressurized ultra-pure water to remove the sanding debris and sandpaper residue. The pressure wash was repeated 3 times, each time followed by drying (all steps in the purged glove box).

The acrylic sleeve and windows in the second iteration (G2) were coated on the inside with ∼80 µm of purified acrylic. Close to 20 grams of clean acrylic were obtained by UV-induced polymerization of vacuum distilled methyl methacrylate, the acrylic monomer. The clean material was then dissolved in a solvent, acetonitrile, which had been purified by vacuum distillation, and applied to the inner chamber surfaces. The coating was cast on the acrylic window, and spin-coated on the cylindrical sleeve, then left to dry (for details see Ref. [15]).

In all three cases, TPB coatings were evaporated on the inner surface of the chamber using the apparatus described in [16]. The coatings on the acrylic windows were deposited from a TPB-filled quartz crucible heated with a nickel-chromium wire. The coating on the acrylic sleeve was deposited from a TPB filled NiCr mesh installed along the cylinder axis. The crucible, NiCr mesh and heater were washed beforehand in 10% nitric acid followed by

ultra-pure water, in order to remove any traces of surface radon daughter activity.

For the G2 and G3 coatings, the TPB was pre-heated to 150 °C for a few hours to evaporate contaminants with a lower evaporation temperature than TPB (such as volatile organo-metallic compounds of polonium, see [17]) in absence of the substrate. The coating deposition rate and thickness during the final process was monitored by quartz balance deposition monitors.

The coated parts were stored in the dark in order to avoid TPB degradation reported in some literature sources [18].

Finally, the inner chamber was installed in the ultrasonically cleaned DEAP-1 outer stainless steel vacuum chamber, which was then sealed, pumped out and over-pressurized with 18 psi of nitrogen gas to minimize exposure to radon during transportation between Queen's University and the underground site at SNOLAB. Connecting the detector to the DEAP-1 process systems required a ∼30 minute exposure to the ambient air with a ^{222}Rn activity of about 120 Bq m^{-3}.

4.2. Argon purity and radon trap

Argon purification for DEAP-1 is effected with a hot-zirconium SAES getter resulting in argon with sub-ppb-level contamination from volatile hydrocarbons, water vapour, carbon dioxide, oxygen and nitrogen. The argon gas to be filled into the DEAP-1 detector is stored in pressurized bottles. These bottles or the attached armature emanate low levels of radon which is removed with a dedicated radon trap. A tube filled with 10 g of activated carbon spheres (Carboxen®) was placed on the argon inlet between the argon source and the liquefying column. The trap was cooled in a bath of ethanol

and liquid nitrogen to $-110\,^{\circ}\mathrm{C}$ with no transient excursions warmer than $-100\,^{\circ}\mathrm{C}$. Tests of the trap indicate that less than one atom of $^{222}\mathrm{Rn}$ passes the trap and enters the detector during a fill [19].

4.3. Shielding

The detector is shielded against neutrons by a minimum of two layers of ultra-pure water in 30.5 cm cubical polyethylene containers, for a total water shielding thickness of 60 cm, surrounding the whole detector. External gammas and muons, at the level they occur at SNOLAB, are not a major concern for DEAP-1, so no additional gamma-shielding was used.

4.4. Pulse shape discrimination

The time spectrum of the emitted argon scintillation light depends on the linear energy transfer (LET) along the track of the exciting radiation [20]. Pulse shape discrimination thus allows separation of electron recoil interactions and nuclear recoil interactions in the argon which have low and high LET respectively.

DEAP uses the fraction of light emitted during the first 150 ns of a signal as pulse shape discrimination parameter Fprompt. Electron-recoil interactions have an Fprompt value around 0.3, compared to 0.7 for nuclear recoil interactions. The mean and spread of the Fprompt distribution versus energy is determined using a tagged $^{22}\mathrm{Na}$ source (as described in Ref. [5]) for electron recoils and an AmBe neutron source for nuclear recoils.

5. Background Analysis

Fig. 3 shows the location of nuclear recoil like events in the DEAP-1 detector versus the number of detected photoelectrons (PE) for three different detector generations. The Zfit parameter, which is calculated based on the relative amounts of light detected in the two PMTs, indicates the position of events along the axis of the detector joining the two PMTs. The Zfit parameter was calibrated using the back-to-back 511 keV gamma rays from an external ^{22}Na source. A tag NaI detector was held behind the source and tuned to trigger when a backward-going 511 keV gamma was measured. The source and tag detector were scanned along the length of the DEAP-1 active volume, allowing readout to be triggered only on gamma events at a specific z-location within DEAP-1.

Below about 1000 PE, the light yields are 2.4 PE/keV, 4.7 PE/keV and 4.0 PE/keV for G1, G2 and G3 respectively, as determined with ^{22}Na (511 keV) and ^{241}Am (59.5 keV) gamma calibration sources. The light yield and the Zfit calibration are non-linear at higher energies due to saturation of both the PMTs and the read-out electronics.

Four distinct populations of events are visible for each detector generation in Fig. 3: A high energy population evenly distributed across the detector (A), a population ranging in energy from zero up to the high energy population but located mainly near the windows and in the centre of the detector (B), a population at low energies evenly distributed across the detector (C), and a population near the windows of the detector at low energies (D). The origin of each population will be discussed in the following sections. A more detailed discussion can be found in Ref. [21].

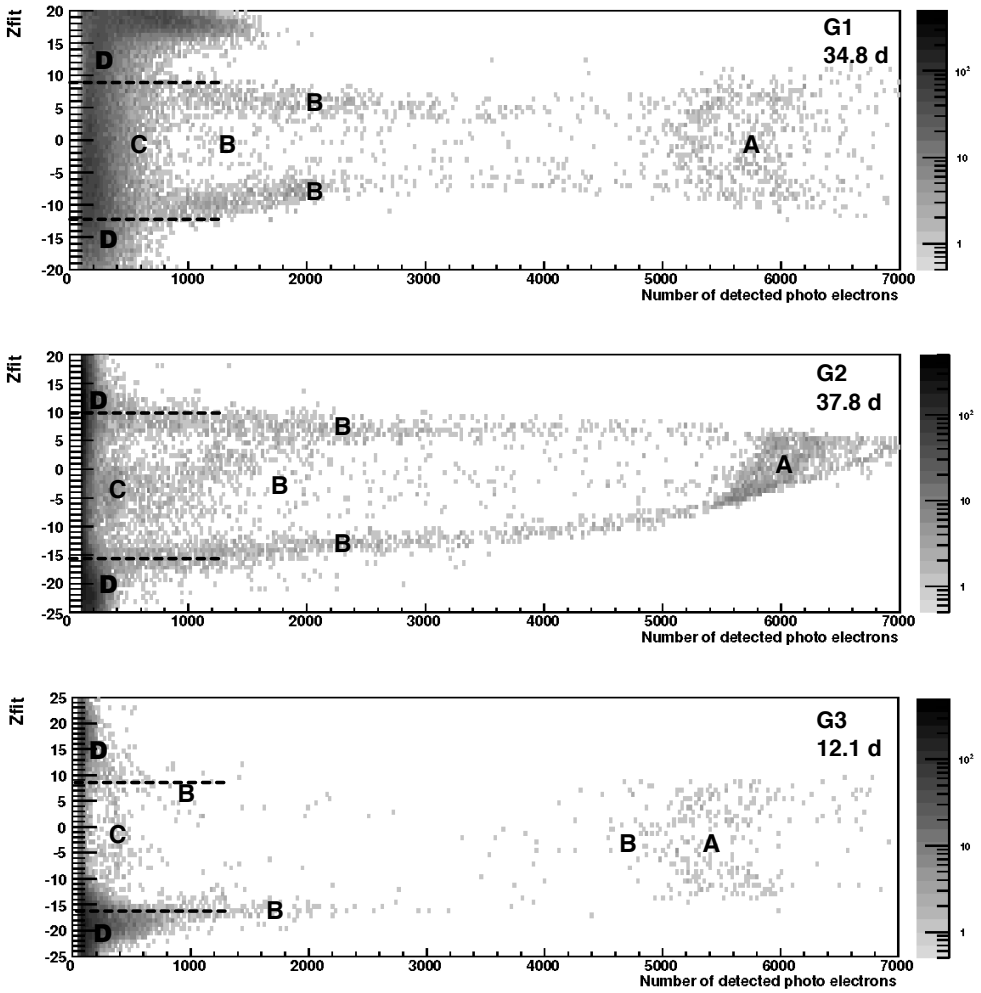

Figure 3: The reconstructed location of nuclear recoil-like events along the axis of the detector (Zfit in units of cm) versus the number of detected photo electrons. The three panels correspond to DEAP-1 detector generations G1 through G3. The number of photo electrons correspond to energies between 0 and 8 MeV. The live-time for each configuration is given in each figure. Dashed lines indicated the approximate location of the acrylic windows for low energy events.

5.1. Tagging radon in DEAP-1

Timing coincidence tags and analysis of the energy spectra indicate that population A in Fig. 3 is from decays of radon and its daughters in the active liquid argon volume.

The polonium daughters of ^{220}Rn and ^{222}Rn have short half-lives, 0.15 s and 183 s respectively. A pair of consecutive events in population A is preliminarily tagged as a ^{220}Rn coincidence if the two events are separated by up to $\Delta t = 0.5$ s, and as a ^{222}Rn coincidence if the pair is separated by 0.5 s to $\Delta t = 500$ s.

To find the number of real coincidences, N_c, the expected number of random coincidences N_r must be subtracted from the number of tagged events N_{tag} and the efficiency of the tag must be taken into account. The number of random coincidences can easily be estimated if the total number of events in population A, N_{all}, is much larger than N_c. This is not the case in much of the DEAP data, especially during the radon calibration spike (discussed later). The actual number of radon coincidences must thus be calculated as

$$N_c = [N_{tag} - N_r]/\epsilon \tag{1}$$

$$= [N_{tag} - (N_{all} - N_c) \cdot (1 - e^{-(N_{all}-N_c)\cdot \Delta t/T})]/\epsilon \tag{2}$$

where T is the live-time of the data taking run and ϵ is the efficiency of the tag. For the time windows used above, the efficiencies are 99.9% and 85% for the ^{220}Rn and ^{222}Rn tags. This equation has no analytic solution, however an iterative solution can be found where

$$N_c^{(0)} = 0 \tag{3}$$

$$N_c^{(n)} = [N_{tag} - (N_{all} - N_c^{(n-1)}) \cdot (1 - e^{-(N_{all}-N_c^{(n-1)})\cdot \Delta t/T})]/\epsilon \tag{4}$$

This converges after 6 to 11 iterations in our data sets.

The timing spectrum of pairs of consecutive events from population A is shown in Fig. 4. The fitted half-lives are those of ^{220}Rn and ^{222}Rn, indicating that these tags are radon coincidences.

The average radon rates found for each detector configuration are presented in Table 1. The rates for each background run in G1 and G2 are shown in Fig. 5. The rates were stable over many months. Data in G2 and G3 were taken with nominal and lower than nominal voltage on the PMTs to increase the dynamic range.

Version	Run time (d)	Number of tags		Rate [10^{-5}Bq]	
		^{222}Rn	^{220}Rn	^{222}Rn	^{220}Rn
G1	34.8	349 ±22	77 ±7	11.6 ±0.7	2.56 ±0.21
G2 LV	14.0	199 ±17	27 ±5	16.3 ±1.4	2.23 ±0.43
G2 NV	37.8	599 ±29	62 ±8	18.3 ±0.9	1.90 ±0.24
G3 LV	13.1	135 ±13	16 ±4	11.6 ±3.5	1.5 ±0.3

Table 1: Number of tagged radon decays in DEAP-1 G1, G2, and G3. LV and NV stand for lower than nominal voltage and nominal voltage runs respectively.

5.2. Radon spectra

Many types of surface backgrounds have energy spectra that reach up to above 5 MeV, the realm of radon alphas. A well understood radon spectrum can thus be used to find limits for the level of surface contaminations.

The full energy alpha spectra are shown in Fig. 6 and Fig. 7. The energy scale was calibrated using the tagged alpha decays from radon and polonium.

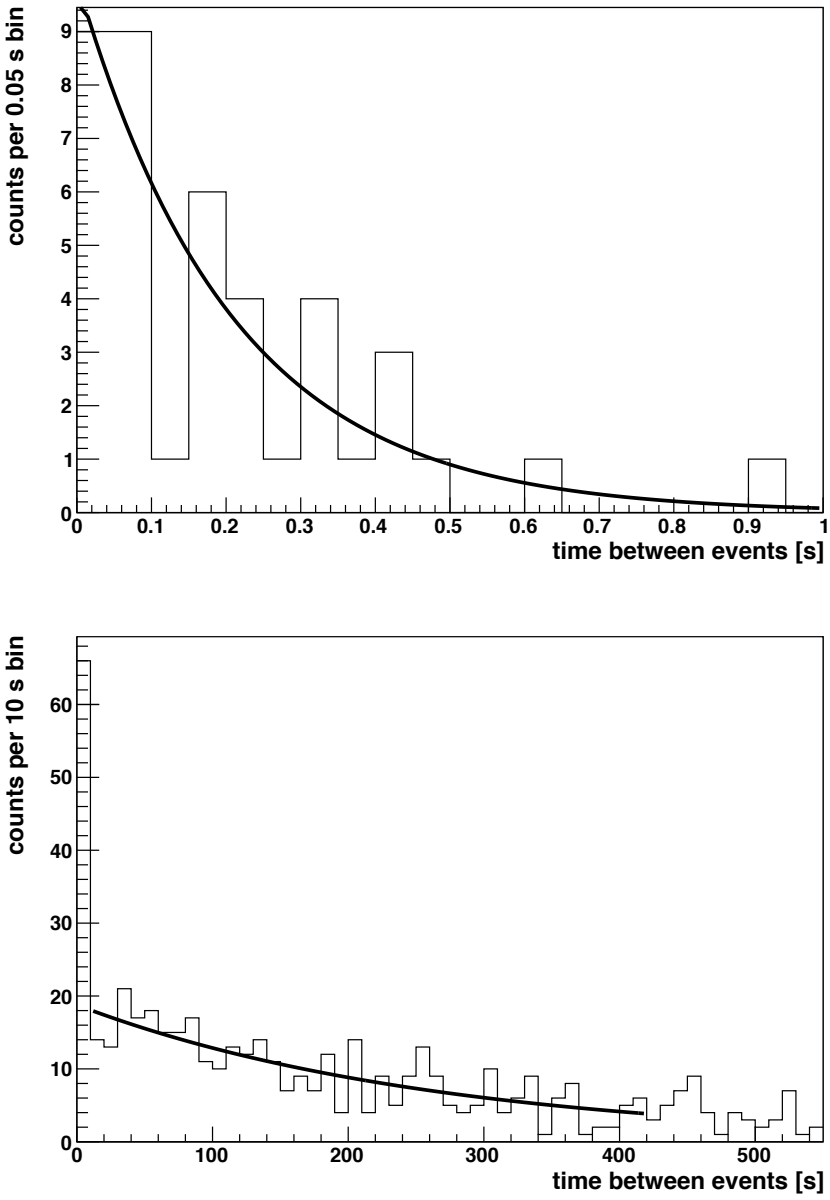

Figure 4: The timing spectrum for events from population A (G2). Top: Up to 1 second, fitting a half-life of 0.14±0.03 s. Bottom: Up to 300 seconds, fitting a half-life of 181±26 s.

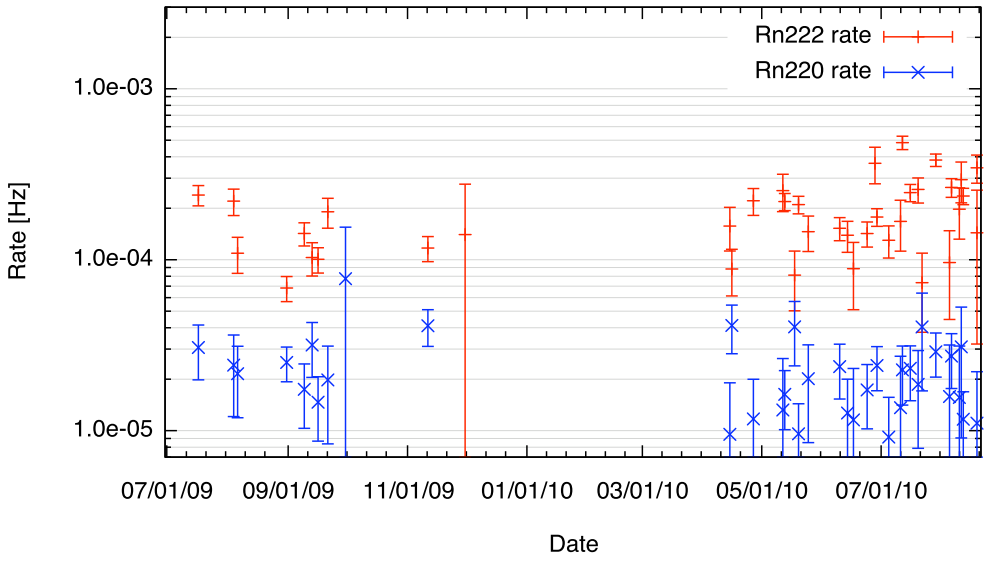

Figure 5: Tagged rates of ^{222}Rn and ^{220}Rn for each background run in G1 (data from 2009) and G2 (data from 2010).

The spectra were fit with a sum of five Gaussians, assuming that all events above 5.2 MeV are due to decays of ^{222}Rn, ^{218}Po, ^{214}Po, ^{220}Rn and ^{216}Po. The ^{212}Bi and ^{212}Po are expected to have very low peak intensities and are disregarded in the fit, because the rate of ^{220}Rn is much lower than that of ^{222}Rn, the chain is split between ^{212}Bi and ^{212}Po, and their rate can be expected to be suppressed by the same amount as that of ^{214}Po (discussed later). The rate of ^{210}Po is strongly suppressed due to the long half-life of ^{210}Pb and it is disregarded as well.

The energies of the peaks and the relative intensity of each peak were fixed, while the number of events in each chain, energy resolution and ^{214}Po scaling factor were fitted out. The number of ^{214}Po events had to be reduced by a scaling factor η to make a good fit. The missing ^{214}Po events can be

found at low energies, the evidence and explanation for this is discussed in the next section.

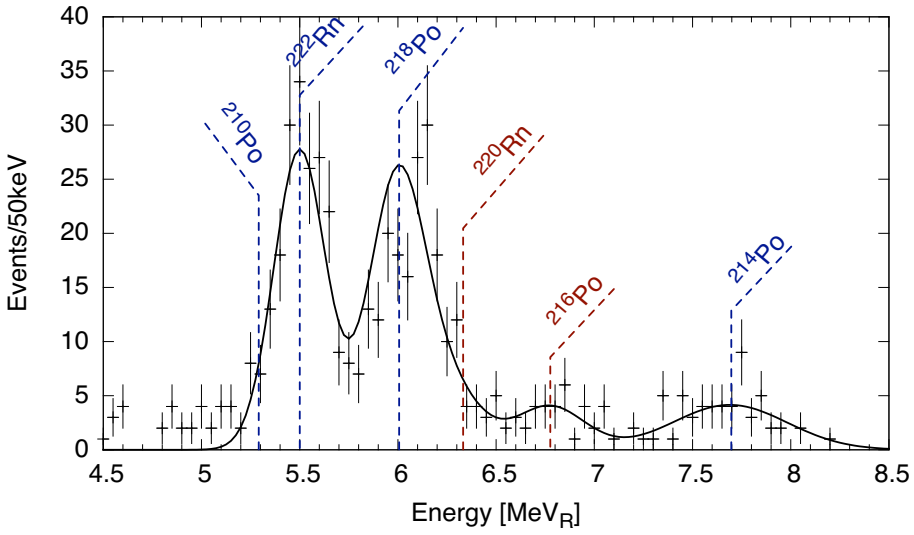

Figure 6: Spectrum of full energy alphas in DEAP-1 G2. The ^{214}Po peak is reduced compared to the ^{222}Rn peak. The missing events can be found at low energies.

The results of the fits are summarized in Table 2.

The fitted number of radon events is consistent with the number of tagged events in Table 1 for both G1 and G2 and for both radon isotopes. In G3, the tagged number of events is 20% lower than the fitted number of events, and the timing spectra are distorted. The reason for this is so far not understood.

To check if any other sources of alpha particles could be contributing to the high energy events in G1 and G2, the total number of tagged events was compared to the number of high energy events. Each tagged event is followed by three more alpha events down the decay chain. The ^{214}Po events however are suppressed by a factor of η, as fitted. We apply the same suppression

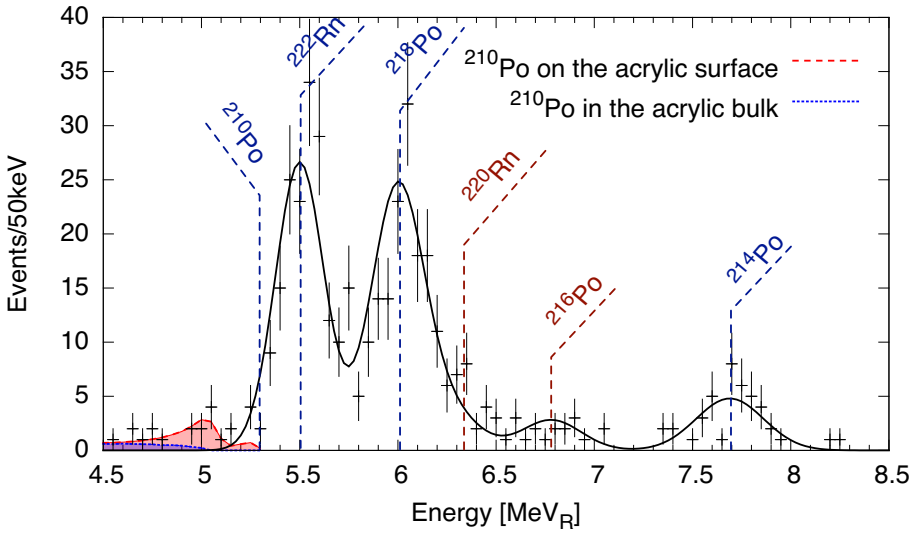

Figure 7: Spectrum of full energy alpha particles from the ^{222}Rn and ^{220}Rn chains in DEAP-1 G3. Also show in the simulated spectrum of ^{210}Po on the acrylic surface, which was fitted to the observed spectrum between 4.5 and 5.2 MeV (the shaded region). The spectrum of ^{210}Po in the acrylic bulk is also drawn, with the normalization found from fitting an intermediate energy range. (See Sect. 5.4.)

	χ^2/NDF	Number of atoms		Resolution	^{214}Po
		^{222}Rn	^{220}Rn	σ/E	scaling factor
G1	1.3	350 ±15	73 ±9	0.033 ±0.002	3.4 ±0.4
G2 LV	1.1	181 ±10	36 ±6	0.025 ±0.002	2.9 ±0.4
G3 LV	1.0	165 ± 9	21 ±4	0.023 ±0.001	4.0 ±0.7

Table 2: Parameters obtained from fitting the full energy alpha spectra (compare Fig. 6 and Fig. 7).

factor to the decays following ^{212}Pb in the ^{220}Rn chain. The number of events identified by the tags is then

$$N_{id} = (2 + 1/\eta) \cdot N_{222Rn} + (2 + 1/\eta) \cdot N_{220Rn} \quad (5)$$

We find that the numbers of events due to other backgrounds are 6± 60 out of 985 for G1, -13± 44 out of 516 for G2 LV and 19± 99 out of 2097 for G2 NV runs. In all cases, the number of unidentified events is consistent with zero and allows for a high energy event rate not caused by radon and daughters of no more than 3.6×10^{-5} Hz.

5.3. Geometric backgrounds

Population B in Fig. 3 arises from alpha decays of radon and its daughters in regions of the detector not completely visible to the PMTs. The geometry of the detector includes small gaps near the windows and near the neck from where only some of the scintillation light can reach the PMTs, so events from these regions have reduced visible energy. This explanation was suggested by GEANT4 Monte Carlo simulations and verified by an injection of ^{222}Rn into DEAP-1 G2.

The radon spike was prepared using radon from SNOLAB air, which has an activity of approximately $120\,\mathrm{Bq\,m^{-3}}$ [11]. Approximately $0.5\,\mathrm{m^3}$ of lab air was pumped through a NaOH trap to remove CO_2; a cold trap at approximately $-50\,^{\circ}\mathrm{C}$ to remove water vapour; and then a trap filled with a porous polymer medium (Chromosorb® 102 manufactured by Supelco, a member of the Sigma Aldrich group) kept at approximately $-110\,^{\circ}\mathrm{C}$ to capture radon. Oxygen and nitrogen passed through all traps. The trapped radon was concentrated in a small trap and then allowed to expand into a

100 cm^3 storage tube. This tube was then attached to the DEAP-1 argon system inlet, which was first pumped of all contaminants and then filled with argon at a higher pressure than the circulation loop. The radon storage tube was opened to the argon inlet and then the argon was opened to the recirculation loop (through a SAES getter) until the pressure equilibrated. The inlet was then closed and re-pressurized. There were four injection cycles within a ten-minute period.

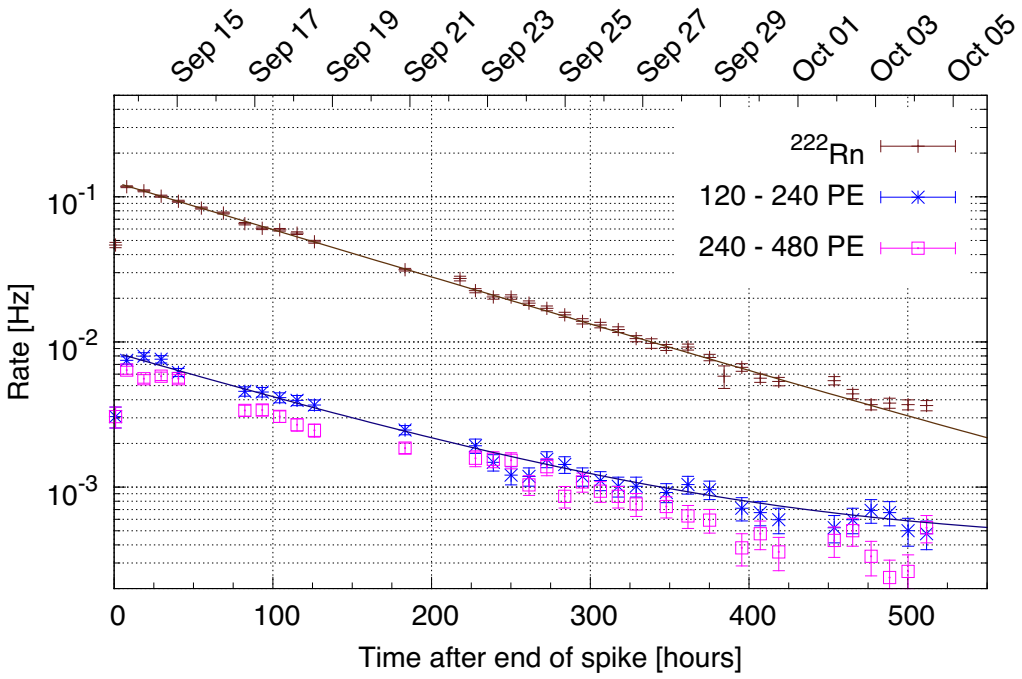

Figure 8: Radon alpha rate and event rate in two low energy windows (corresponding roughly to 25 keVee to 50 keVee and 50 keVee to 100 keVee) versus time after the radon spike. Theoretical decay curves based on the ^{222}Rn lifetime and the constant rate before the spike are also drawn.

The rates of the full energy radon alphas and the population in two low

energy regions were tracked versus time as shown in Fig. 8. The low-energy region rate decreases with a decay constant consistent with ^{222}Rn, indicating that these low energy events are in fact caused by radon decays.

The redesign of the detector chamber from G2 to G3, to include a neck plug and more tightly fitting windows was based on these findings.

5.4. Surface backgrounds

Monte Carlo simulation indicates that the events of population C in Fig. 3 are from ^{214}Po alpha decays on the TPB surface. The ^{214}Po is in the ^{222}Rn decay chain and there is ample time for the lead and bismuth isotopes preceding ^{214}Po to float through the argon and impinge on a detector surface. All three of these elements tend to adhere to surfaces, making it likely that ^{214}Po decays from a surface.

The geometry of surface backgrounds in general is shown in Fig. 9. Paths that lead to light emission are labelled F1 to F3. In the simulation, both the liquid argon and the TPB scintillate. The light yield of TPB under alpha particle excitation was taken from Ref. [16]. The scintillation in acrylic was assumed to be negligible.

Spectra simulated with a SRIM [22] based code, taking into account the energy of the recoil nucleus but no detector resolution effects, are shown in Fig. 10 and Fig. 11. The simulation includes the different TPB thicknesses on the acrylic windows and sleeve (this is the reason for the double peak structure at F3 in Fig. 11). Features in the spectra are labeled with the same names as the paths in Fig. 9 that generate them.

The ^{214}Po spectrum in Fig. 10, corresponding to situation c) in Fig. 9, has a peak at low energies (F1) at about 70 keVee. The lowest energy an

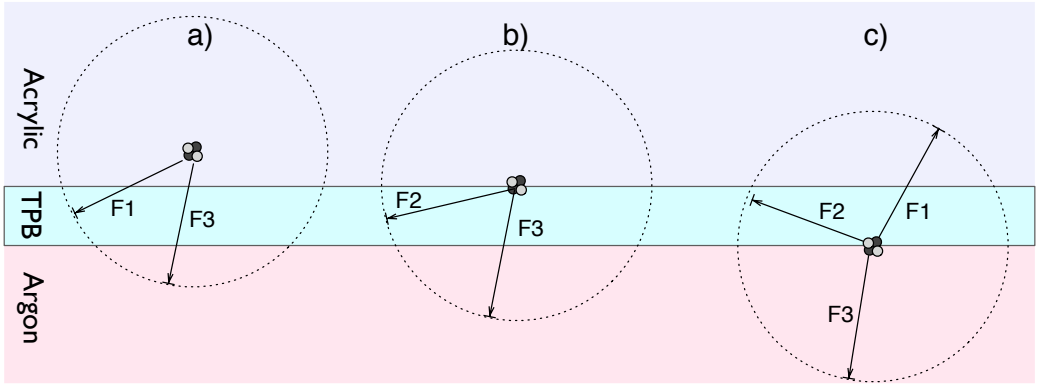

Figure 9: Sketch of possible paths that lead to light emission for an alpha particle emitted in the bulk acrylic (a), on the acrylic surface (b), and on the TPB inner surface (c).

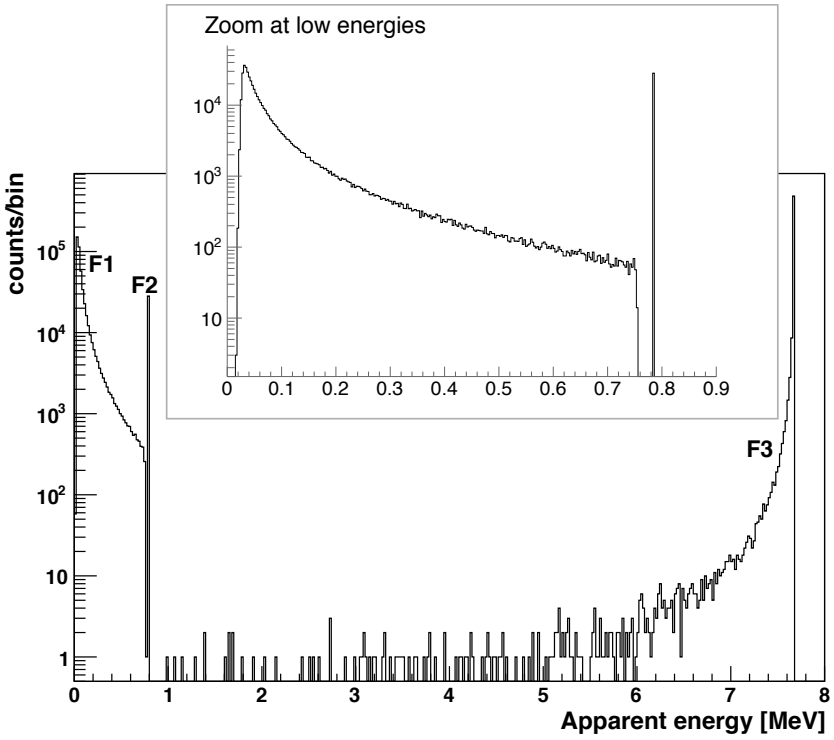

Figure 10: Simulated spectrum of ^{214}Po alpha decays from just below the inner surface of the TPB (situation (c) in Fig. 9).

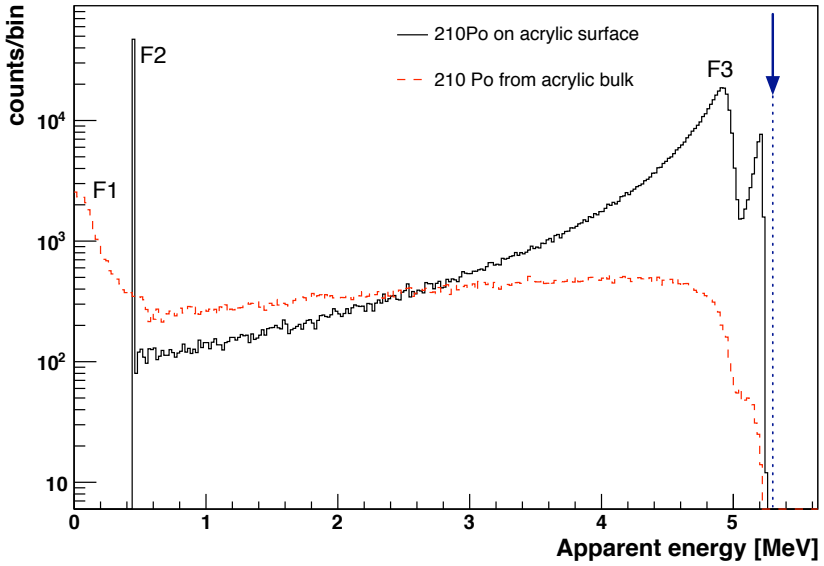

Figure 11: Simulated spectra of ^{210}Po on the acrylic surface (situation (b) in Fig. 9) and in the bulk acrylic (situation (a) in Fig. 9). The full energy of the alpha particle is indicated by the arrow.

event can have in this case corresponds to the shortest path through the TPB. Any isotope emitting a lower energy alpha will have a similar peak at a slightly higher energy, since the energy loss increases for lower kinetic energy particles. This means that given a smooth, uniform thickness TPB layer and infinite energy resolution, there is a low energy cutoff below which no such surface events occur.

Relatively long lifetimes of ^{214}Pb and ^{214}Bi (see Fig. 2) allow them to freely float around the detector and eventually adhere to the TPB surface. Then, in the case of a perfectly smooth surface exactly half of the decays of their decay daughter, ^{214}Po, should send the alpha particle into the TPB, while the other half send it into the argon. If all ^{214}Po is on the TPB surface, the number of events in the full energy liquid argon scintillation peak is then equal to the number of events in the low energy TPB scintillation peak, and both added are equal to the number of ^{222}Rn decays. The ^{214}Po scaling factor used in the spectrum fits would then be exactly two.

The ratio is different for rough surfaces, where some of the particles emitted into the argon can travel a short distance and then enter TPB again. This is the reason why the ^{214}Po scaling factor (η) found from fitting the full energy alpha spectra is larger than two.

A minimum visible energy also exists for alpha decays that happen on a perfectly smooth acrylic surface. The paths labeled F3 all end in the liquid argon, so that most or all of the alpha's energy is visible. The lowest energy event happens when the alpha loses all its energy in the TPB (F2 paths). For rough surfaces or when straggling is considered, events with lower visible energy are possible.

The most problematic backgrounds are then from alpha decays in the acrylic bulk or the TPB bulk, which lead to events down to 0 keV even under the first order approximation of a smooth surface without straggling.

We have developed a detailed GEANT4 based model to study the combined effects of surface roughness, contamination and straggling. It has been successfully employed to re-interpret recent results by CRESST-II and suggested a simple explanation for the reported excess of low energy events [23]. In the case of DEAP-1, for the TPB surface contamination, no significant enhancement at the low energy end of the spectrum occurs, mainly because of the finite minimum thickness of the TPB coating, responsible for the low energy cutoff in the spectrum. We have confirmed that for a realistic choice of TPB surface roughness parameters informed by surface profile scans (a sinusoidal model with 20% thickness variation and 10 µm period waviness), the resulting spectra are well approximated by the ideal case as long as as the coating is free of pinholes. This can be explained by the fact that the roughness scale is significantly smaller than the range of alpha particles. Note that this does not change the finding that the number of alphas emitted into the TPB and into the argon is divided unevenly. Surface roughness plays more significant role for ^{210}Po activity on the acrylic surface and could potentially introduce low energy tails in the spectrum. However, this possibility is excluded by the contamination limits discussed in the next section.

5.5. Limits on surface contamination

The high energy spectrum from G3 data was fit with the simulated spectrum of ^{210}Po on the acrylic (see Fig. 11 and 7) to determine the number of ^{210}Po decays necessary to cause events around 5 MeV with the observed rate.

The resulting contamination was found to be $3.1 \times 10^{-8}\,\mathrm{Bq\,cm^{-2}}$, assuming all the events around 5 MeV are due to this source.

Events at intermediate energies between 1 and 4 MeV near the center of the detector come from ^{210}Po on and in the acrylic. The energy calibration at these energies has large uncertainties and the number of events observed there is small (around 25). The spectrum was therefore not fit, but the number of events integrated. Then the fraction of ^{210}Po decays in the acrylic that lead to events in this energy range was determined from the simulation and used as a correction factor on the observed number of events. Assuming that all these events are from ^{210}Po in the bulk acrylic, its concentration is $(3.2\pm0.6)\cdot10^{-5}$ Bq/cm^3 or $(1.6\pm0.3)\cdot10^{-19}$ g/g. Based on this estimate, the number of ^{210}Po events expected in the low energy part of the spectrum, i.e. between 50 and 200 keVee, is about 2 orders of magnitude below the measured number of events (as will be discussed later, the dominant contribution at low energies is attributed to ^{214}Po).

These results can be interpreted as upper limits. Some geometric background events could be contributing to the event rate around 5 MeV, and some of the ^{210}Po events from the acrylic surface have energies between 1 and 4 MeV.

5.6. Window backgrounds

Event population (D) in Fig. 3, near both windows at energies up to about 100 keVee, was observed in every iteration of the DEAP-1 detector but its origin is unclear. The geometric background events from alpha particles emitted near the windows reconstruct at a location slightly closer to the detector centre than the window backgrounds, indicating that the window

events might come from the glass rather than the acrylic windows.

In order to reduce the rate of these events, a 10 cm long cylinder centred on the middle of the detector is defined as the fiducial volume.

5.7. Background rates

A summary of background event rates is shown in Table 3. The rates correspond to a cut on the pulse shape discrimination parameter that has an efficiency of 50% for nuclear recoil events, as calibrated with an AmBe neutron source.

	Background rates [µHz]	
detector	120-240 PE	50-100 keV$_{ee}$
G1	47 ±4	47 ±4
G2	23 ±3	30 ±3
G3	10 ±4	7 ±4

Table 3: Background rates at 50% nuclear recoil efficiency, along 10 cm of the detector corresponding to a fiducial volume of 2.5 kg. The rates are shown in the window of TotalPE which is of interest for PSD analysis, as well as in a common energy window. The different detector generations had different light yields, so that the same TotalPE window does not correspond to the same energy window between generations.

6. The low energy background spectrum

The low energy spectrum of the lowest background detector, G3, is shown in Fig. 12 for 85±5% nuclear recoil efficiency. The events in that spectrum are due to three main sources: PSD leakage, window leakage and ^{214}Po on the TPB surface.

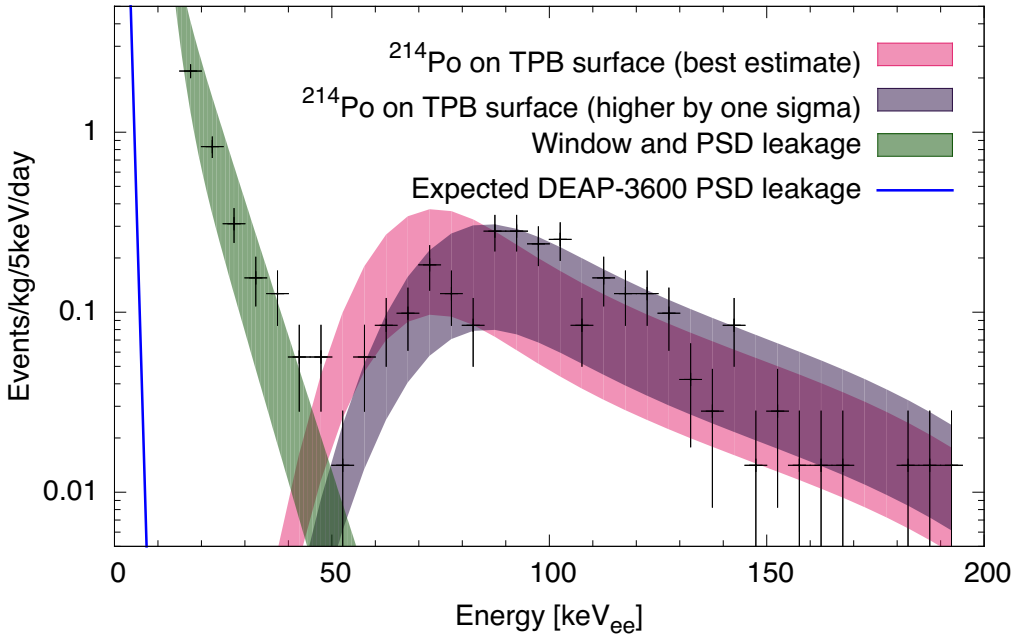

Figure 12: G3 low energy background spectrum with a PSD cut that has 85±5% recoil efficiency. The estimated rate of window and PSD leakage into the data region is drawn in medium grey (green). The light grey (pink) band shows the expected location of the peak from ^{214}Po on the TPB surface (compare Fig. 10) both with best estimate parameters for the TPB thickness, TPB scintillation efficiency and nuclear recoil quenching factor in argon. The shaded region corresponds to one sigma above and below the best estimate value for the rate. The dark grey (purple) band indicates the one sigma uncertainty of the peak location.

PSD leakage refers to electromagnetic background events that the pulse shape discrimination method is not able to separate from nuclear recoil events. The amount of PSD leakage is determined mainly by photo electron statistics and thus increases exponentially towards lower energies. The PSD leakage rate per energy bin was determined using dedicated PSD data runs with a tagged ^{22}Na source, which provided data up to about 25 $\mathrm{keV_{ee}}$, and it was extrapolated to higher energies from there.

Window leakage refers to events (from population D in the previous section) that should reconstruct on the windows of the detector, but which, also due to low photoelectron statistics at low energies, reconstruct in the fiducial volume. The amount of leakage into the region of interest was extrapolated for each energy bin by fitting the event position distribution with two gaussians near the windows on top of a constant rate. The two gaussians were then integrated over the region of interest to estimate how many window events leak into this region. Both leakage contributions are included in the medium grey (green) band in Fig. 12.

The light and dark grey (pink and purple) bands in Fig. 12 are the result of the simulation described in the previous section, for ^{214}Po on the TPB surface. The number of events in that spectrum is determined by the number of ^{214}Po events missing at high energies and the efficiency of the region-of-interest cuts. The uncertainty is dominated by the statistical uncertainty on the high energy alpha rate.

The peak includes a contribution from the TPB induced alpha scintillation and from the scintillation of argon due to the recoil nucleus. Its location depends on the TPB thickness, TPB scintillation yield (ϵ_{tpb}) for alphas and

the quenching factor for nuclear recoils in argon (q). The simulation returns the energy deposited in TPB E_{tpb}, the scintillation light of which is interpreted in terms of the liquid argon light yield for electrons (ϵ_{lar}). The apparent event energy in keV$_{ee}$ is then

$$E_{app} = \frac{E_{tpb}\epsilon_{tpb}}{\epsilon_{lar}} + q \cdot E_{r,lar} \tag{6}$$

where $E_{r,lar}$ is the energy of the recoil nucleus going into the liquid argon. All three parameters have uncertainties associated with them. The one sigma uncertainty in one direction on these parameters ($E_{app} + \Delta E_{app}$) is indicated by the dark grey (purple) band.

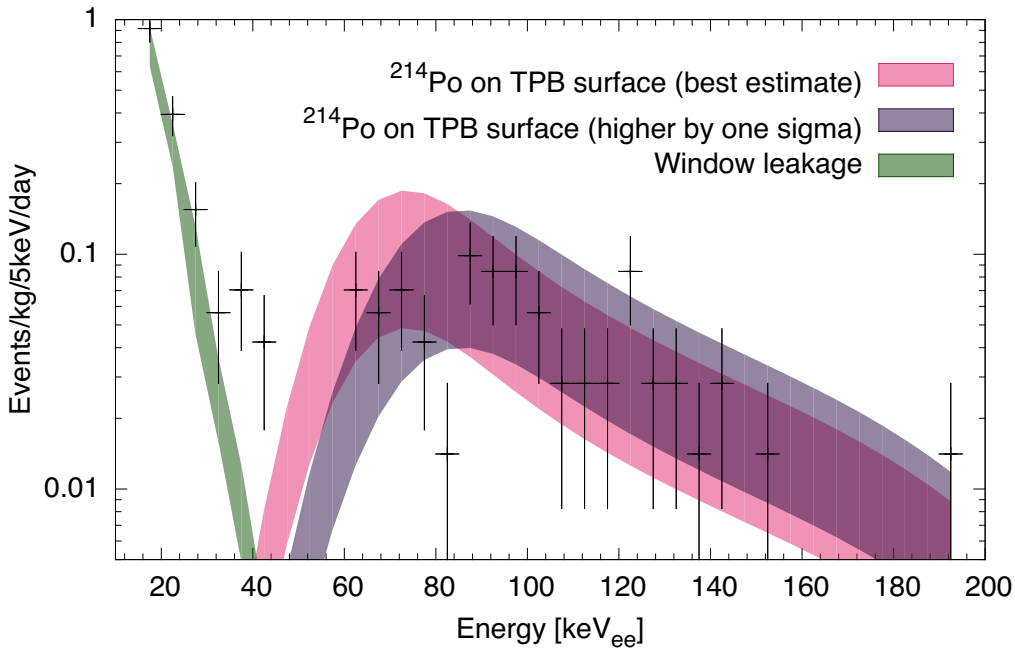

Figure 13: G3 low energy background spectrum. Same as Fig. 12, but with 50±5% recoil efficiency.

The rate of ^{210}Po decays on the TPB surface, following down the decay

chain from ^{214}Po, is strongly suppressed due to its long half-life, and contributes only a couple of events to the spectrum. Some ^{218}Po adheres to the TPB surface as well, but only a small number of these events are missing in the high energy spectra so that this is also negligible.

The spectrum for 50±5% recoil efficiency is shown in Fig. 13. The medium grey (green) band includes only window event leakage, since not enough data was available to extrapolate the gamma leakage here.

7. Discussion

Radon and its daughters cause three distinct types of alpha backgrounds. If the decay happens in the active liquid argon volume, a full energy event is observed which can be readily discriminated from a WIMP event based on its energy. A sustained full energy radon rate between 110 and 180 µBq (or 16 to 26 µBq kg^{-1}) for ^{222}Rn and between 15 and 25 µBq for ^{220}Rn was observed in each iteration of DEAP-1. The radon is believed to come from the argon process system.

A small number of the radon decays occurs in liquid argon volumes outside the active volume, near the windows and the neck of the detector, from where only a fraction of the scintillation light can reach the PMTs. These geometric background events have an energy spectrum reaching down to the energy threshold of the detector. A ^{222}Rn spike demonstrated the relation between low energy backgrounds and radon rate, and modification of the detector to reduce the gap sizes near the window and neck resulted in reduced low energy backgrounds.

The ^{214}Po from the ^{222}Rn chain adheres to the TPB so that only a fraction

of the alpha particles are emitted into the liquid argon, as evident from the reduced intensity of the ^{214}Po peak in the full energy spectra. Because the TPB forms a rough surface, the peak intensity is reduced more strongly than it would be for perfectly smooth surface. When the alpha particle is emitted into the TPB and the recoil nucleus into the liquid argon, events with visible energies between 60 and 200 keVee result.

Other surface backgrounds are from ^{210}Po on the acrylic surface and in the acrylic bulk. ^{210}Po is expected to be present in acrylic because the beads acrylic is typically made from are saturated in ^{222}Rn, and the acrylic chamber was in contact with air for a few minutes during production. Limits for these contaminations were obtained.

The events in the low energy background spectrum can be explained by PSD and window leakage up to about 50 keVee and by surface ^{214}Po between 50 and 200 keVee. The expected contribution of the ^{210}Po in the bulk acrylic to the low energy spectrum, based on the rate observed at intermediate and high energies, is two orders of magnitude below the observed background rates.

The higher projected light yield and improved electronic noise level in DEAP-3600 will strongly reduce the PSD leakage, while the simpler geometry is expected to eliminate the window events. The medium grey (green) band in Fig. 12 will thus be shifted to the blue line shown in the same figure. The ^{214}Po surface events are at the upper end of the energy region of interest in DEAP-3600. They will lead to less background rate in the region of interest than the design goal if the radon rate is kept below 0.1 mBq

8. Conclusions

The origin of the low energy background events in DEAP-1 was explained in terms of PSD leakage, geometrical gap alphas, surface ^{214}Po and window leakage. This work confirms that the design and the specified radiopurity of DEAP-3600 are conservative and that they will allow to meet the background target of less than 0.6 event in 3 tonne-years (for detailed background budget see [8]).

The event class leading to window leakage is not expected to exist in DEAP-3600 due to the different detector geometry. The neck in DEAP-3600 was designed to strongly reduce the gap alpha rate, and the planned argon purity with regards to radon will keep the surface ^{214}Po event rate significantly below the required level (as the combined visible energy from nuclear recoils and alphas from ^{214}Po decays is above the upper bound of the energy region of interest relevant for the WIMP search). The latter finding also confirms that the TPB scintillation light yield under alpha particle excitation at the liquid argon temperature (87 K) is consistent with our earlier room temperature measurement [16].

Backgrounds caused by radioactive radon daughters embedded in acrylic have been studied in detail by means of Monte Carlo simulations and are well understood. We have obtained competitive radiopurity limits for acrylic (coming from an uncontrolled source), which are already sufficient to run the DEAP-3600 with reduced target mass (assuming very conservative position reconstruction resolution). Significant improvement in acrylic purity is expected due to the undertaken acrylic quality assurance and assay program and due to in-situ resurfacing of the inner acrylic surface (for details see [24]).

Finally, the PSD leakage in DEAP-3600 will be strongly suppressed with higher light yield and less electronic noise than is experienced in DEAP-1.

9. Acknowledgements

This work has been supported by the Canada Foundation for Innovation (CFI), the Natural Sciences and Engineering Research Council of Canada (NSERC) and the Ontario Ministry of Research and Innovation (MRI). The High Performance Computing Virtual Laboratory (HPCVL) has provided us with CPU time, data storage and support. We would also like to thank David Bearse for invaluable technical support and the SNOLAB staff for on-site support. The work of our co-op and summer students is gratefully acknowledged.

References

[1] D. N. McKinsey, The Mini-CLEAN experiment, Nuclear Physics B (Proc. Suppl.) 173 (2007) 152–155.

[2] R. Brunetti, E. Calligarich, M. Cambiaghi, F. Carbonara, A. Cocco, C. D. Vecchi, R. Dolfini, A. Ereditato, G. Fiorillo, L. Grandi, G. Mangano, A. Menegolli, C. Montanari, M. Prata, A. Rappoldi, G. L. Raselli, M. Roncadelli, M. Rossella, C. Rubbia, R. Santorelli, C. Vignoli, WARP liquid argon detector for dark matter survey, New Astronomy Reviews 49 (2-6) (2005) 265–269.

[3] A. Wright, for the DarkSide collaboration, The DarkSide Program at LNGS, arXiv 1109.2979.

[4] M. G. Boulay, A. Hime, Direct WIMP Detection Using Scintillation Time Discrimination in Liquid Argon, arXiv 0411358 (2004) 11358.

[5] M. Boulay, B. Cai, M. Chen, V. Golovko, P. Harvey, R. Mathew, J. Lidgard, A. McDonald, P. Pasuthip, T. Pollman, P. Skensved, K. Graham, A. Hallin, D. McKinsey, W. Lippincott, J. Nikkel, C. Jillings, F. D. B. Cleveland, I. Lawson, Measurement of the scintillation time spectra and pulse-shape discrimination of low-energy beta and nuclear recoils in liquid argon with DEAP-1, arXiv 0904.2930v1.

[6] W. H. Lippincott, K. J. Coakley, D. Gastler, A. Hime, E. Kearns, D. N. McKinsey, J. A. Nikkel, L. C. Stonehill, Scintillation time dependence and pulse shape discrimination in liquid argon, Phys. Rev. C 78 (2008) 035801.

[7] D. Gastler, E. Kearns, A. Hime, L. Stonehill, S. Seibert, J. Klein, W. Lippincott, D. McKinsey, J. Nikkel, Measurement of scintillation efficiency for nuclear recoils in liquid argon, Physical Review C 85 (6) (2012) 065811.

[8] M. G. Boulay (for the DEAP collaboration), DEAP-3600 Dark Matter Search at SNOLAB, arXiv 1203.0604.

[9] F. Duncan, A. J. Noble, D. Sinclair, The Construction and Anticipated Science of SNOLAB, Annual Review of Nuclear and Particle Science 60 (1) (2010) 163–180.

[10] G. J. Davies, C. H. Lally, W. G. Jones, N. J. T. Smith, UV quantum ef-

ficiencies of organic fluors, Nuclear Instruments and Methods in Physics Research Section B 117 (1996) 421.

[11] SNOLAB, User's handbook, Tech. rep., SNOLAB (2006).

[12] I. Lawson, B. Cleveland, Low background counting at SNOLAB, in: Topical workshop on low radioactivity techniques (LRT) 2010, AIP Conf. Proc. 1338, 2011, pp. 68–77.

[13] R. Heaton, Neutron shielding calculations for the SNO detector, Master's thesis, Queen's University (1988).

[14] M. Wojcik, Measurement of radon diffusion and solubility constants in membranes, Nuclear Instruments and Methods in Physics Research Section B 61 (1) (1991) 8–11.

[15] M. Kuźniak, Acrylic purification and coatings, in: Topical workshop on low radioactivity techniques (LRT) 2010, AIP Conf. Proc. 1338, 2011, pp. 101–108.

[16] T. Pollmann, M. Boulay, M. Kuźniak, Scintillation of thin tetraphenyl butadiene films under alpha particle excitation, Nuclear Instruments and Methods in Physics Research Section A 635 (1) (2011) 127–130.

[17] H. Mabuchi, On the volatility of some polonium compounds, Journal of Inorganic and Nuclear Chemistry 25 (1963) 657–660.

[18] C. S. Chiu, C. Ignarra, L. Bugel, H. Chen, J. M. Conrad, B. J. P. Jones, T. Katori, I. Moult, Environmental Effects on TPB Wavelength-Shifting Coatings, arXiv 1204.5762.

[19] E. O'Dwyer, Radon Background Reduction in DEAP-1 and DEAP-3600, Master's thesis, Queen's University (Dec. 2010).

[20] A. Hitachi, T. Takahashi, N. Funayama, K. Masuda, J. Kikuchi, T. Doke, Effect of ionization density on the time dependence of luminescence from liquid argon and xenon, Physical Review B (Condensed Matter) 27 (1983) 5279.

[21] T. Pollmann, Alpha backgrounds in the DEAP Dark Matter search experiment, Ph.D. thesis, Queen's University (2012).

[22] J. Ziegler, M. Ziegler, J. Biersack, SRIM - The stopping and range of ions in matter (2010), Nuclear Instruments and Methods in Physics Research, Section B: Beam Interactions with Materials and Atoms 268 (11-12) (2010) 1818–1823.

[23] M. Kuźniak, M. G. Boulay, T. Pollmann, Surface roughness interpretation of 730 kg days CRESST-II results, Astroparticle Physics 36 (1) (2012) 77–82.

[24] B. Cai, M. Boulay, B. Cleveland, T. Pollmann, Surface backgrounds in the DEAP-3600 dark matter experiment, in: Topical workshop on low radioactivity techniques (LRT) 2010, AIP Conf. Proc. 1338, 2011, pp. 137–146.